Object-based 3D binary reconstruction from sparse projections in cone beam CT: Comparison of three projection operators

Ahmed Oukili, Jean-Claude Nunes, Chen Yang, Limin Luo, Christine Toumoulin

OBJECT-BASED 3D BINARY RECONSTRUCTION FROM SPARSE PROJECTIONS IN CONE BEAM CT: COMPARISON OF THREE PROJECTION OPERATORS

A. Oukili[1,2,4], *J.-C. Nunes*[1,2,4], *Y. Chen*[1,3,4], *L. Luo*[3,4], *and C. Toumoulin* [1,2,4]

[1] INSERM, U1099, Rennes, F-35000, France,
[2] Université de Rennes 1, Laboratoire Traitement du Signal et de l'Image (LTSI), Rennes F-35000, France,
[3] Laboratory of Image Science and Technology, SoutEast University, Nanjing, China,
[4] Centre de Recherche en Information Biomédicale Sino-Francais (LIA CRIBs), Rennes, F-35000, France.

jean-claude.nunes@univ-rennes1.fr

ABSTRACT

We present herein a level set approach to the X-ray tomography problem with sparse projection data and study the impact of the projection operator on the binary reconstruction accuracy and computation time. The comparison is carried out on three projectors: the Separable Footprint (Trapeze-Trapeze, SF-TT) [3], a classical Ray-driven (RD) and a Simplified version of the Distance-Driven (SDD) projector respectively. The performance, are evaluated for each operator, on a binary 3D Shepp-Logan phantom by varying the number of projections from 5 to 13, and considering noise free and noisy cone beam projection data.

Index Terms— cone-beam geometry, projection operator, 3D iterative Reconstruction, object-based reconstruction, level set.

1. INTRODUCTION

Cone Beam Computed tomography is becoming more and more attractive due its capability to integrate the intervention room and provide intraoperative imaging. The imaging system is composed of a gantry that rotates around the patient and on which an X-ray source and flat detector are fixed. During rotation, a sequence of image projections can be obtained (between 100 and 200), which are then exploited to get a 3-D reconstruction of the organs of interest. Many studies have been conducted to reduce radiation dose and the acquisition number [1]. We suggest here reducing the patient dose by limiting the projection number during a scan. As a consequence, the 3-D reconstruction from a few number of projections becomes strongly ill-posed. Works reported in the literature makes use of iterative methods to solve this problem [1, 2].The latter relies on the computation of forward and backward projections and the quality of this reconstruction is highly dependent on the accuracy of the corresponding system matrix. Basic operators include voxel [6, 7], splatting [3], ray-driven (RD) [5], Separable Footprint (Trapeze-Trapeze, SF-TT) [3] and distance driven (DD) [8, 4] approaches. Our contributions concern two phases (presented in Section 2): Simplified version of the Distance-Driven (SDD) and a level set approach to perform the 3D binary tomographic reconstruction. Indeed, in binary case, object-based reconstruction approaches using the level set method, have shown promising results compared to classical methods since this simultaneous segmentation and reconstruction leads to improved results [9]. We studied in section 3 the binary reconstruction obtained from each projection operator (SF-TT, RD and SDD), in varying the number of projections from 5 to 13, and considering noise free and noisy cone beam projection data.

2. METHOD

2.1. Cone-Beam 3D System Model

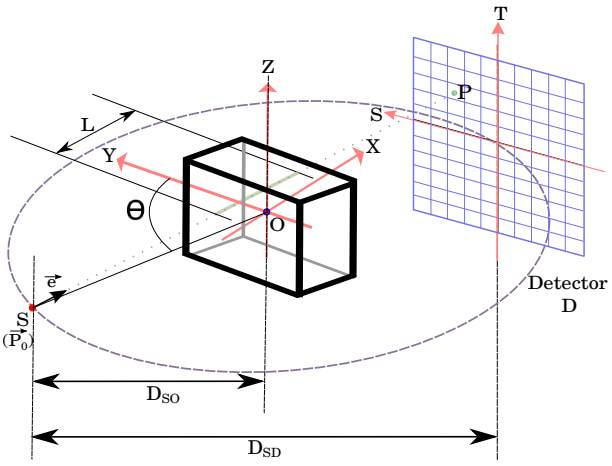

Fig. 1. Acquisition parameters of axial 3D cone-beam flat detector geometry.

3D object f is located between the X-ray source S and the flat-detector which is at a distance D_{SD} from S. The source-detector rotates around Z-axis on which the 3D object is fixed (Fig.1). In order to perform the geometric calculation, we define a system of three-dimensional Cartesian coordinates, $(o, \vec{i}, \vec{j}, \vec{k})$, such as $\left\|\vec{i}\right\| = \Delta_x$, $\left\|\vec{j}\right\| = \Delta_y$, and $\left\|\vec{k}\right\| = \Delta_z$, and another planar coordinate system fixed on the detection grid, consisting of two orthogonal axes, S and T, such as T is parallel to OZ. $(\Delta_x, \Delta_y, \Delta_z)$ and (Δ_s, Δ_t) represent respectively the voxel and pixel sizes.
After the referential definition of rotational acquisition system, first begin by determining the exact value of a projection point $P(s, t; \theta)$ (eq.2), taking into account the cone-beam geometry, and the source position $\vec{P}_0$:

$$\vec{P}_0 = \begin{pmatrix} -D_{SO}\sin(\theta) \\ D_{SO}\cos(\theta) \\ 0 \end{pmatrix} \quad (1)$$

where, D_{SO} denotes the source to rotation center, and θ denotes angle of the source point counter-clockwise from the Y axis.

$$P(s,t;\theta) = \int_{\chi(s,t,\theta)} f(x,y,z)d\chi \tag{2}$$

for which, the integral is along the line segment χ (eq.3), and (s,t) denote the detector coordinates.

$$\begin{aligned}\chi(s,t,\theta) &= \{\vec{P}_0 + l\vec{e} : l \in [0, L_p]\} \\ L_p &= \sqrt{D_{SD}^2 + s^2 + t^2}\end{aligned} \tag{3}$$

where $\vec{e}$ is the direction of the line $\chi(s,t,\theta)$ connecting the source S to the point P:

$$\vec{e} = \frac{\vec{P}-\vec{P}_0}{\|\vec{P}-\vec{P}_0\|} = \begin{pmatrix} \sin\varphi\cos\beta \\ -\cos\varphi\cos\beta \\ \sin\beta \end{pmatrix} \tag{4}$$

where $\beta = -arctg(\frac{t}{\sqrt{s^2+D_{SD}^2}})$ and $\varphi = arctg(\frac{s}{D_{SD}}) + \theta$ denotes respectively the azimuthal and polar angle of the ray from $\vec{P}_0$ to $\vec{P}$. After determining the mathematical expression of a detection point, we identify the value detected by each pixellic surface $\bar{g}_\theta\,[s_k,t_l]$ as:

$$\bar{g}_\theta\,[s_k,t_l] = \int_{\Delta_s}\int_{\Delta_t} h(s_k - s, t_l - t)P(s,t;\theta)dsdt \tag{5}$$

where, (s_k,t_l) represents the centers of detector cell for:
$k = 0,...,N_s-1$, $l = 0,...,N_t-1$, $s_{(k+1)} - s_k = \Delta_s$, and $t_{(l+1)} - s_l = \Delta_t$. h is the detector blur which depends only on coordinates (s,t). Taking into consideration the continuous representation of our 3D discrete object (eq. 6) (which will be defined as a weighted sum of basis function $b_{\vec{\Delta}}$), we can calculate cone-beam footprint $q(s,t;\theta;\vec{n})$ of the n^{th} basis function:

$$f(\vec{x}) = \sum_{\vec{n}} f\,[\vec{n}]b_{\vec{\Delta}}\,(\vec{x} - c\,[\vec{n}]) \tag{6}$$

where $c\,[\vec{n}]$ denotes the center of the n^{th} basis function.

$$q(s,t;\theta;\vec{n}) = \int_{\chi(s,t;\theta)} b_{\vec{\Delta}}\,(\vec{x} - \vec{c}[\vec{n}])\,d\chi \tag{7}$$

Finally, for a projection angle θ, the coefficient linking the n^{th} basis function with a pixel indexed by (s_k,t_l) is determined as:

$$a_\theta\,[s_k,t_l;\vec{n}] = \int_{\Delta_s}\int_{\Delta_t} h(s_k - s, t_l - t)q(s,t;\theta;\vec{n})dsdt \tag{8}$$

However, the exact calculation of $a_\theta\,[s_k,t_l;\vec{n}]$ remains difficult and computationally expensive, hence the necessity to make approximations. The two following sections explain the two different approximation methods.

2.2. Separable Footprint Projector : Trapeze-Trapeze (SF-TT)

For the SF-TT method proposed by Long et al. [3], we consider a simple model for the basis function $b_{\vec{\Delta}}$:

$$\begin{aligned} b_{\vec{\Delta}}(\vec{x} - c\,[\vec{n}]) &= b_0((\vec{x} - c\,[\vec{n}])\emptyset\vec{\Delta}) \\ b_0(\vec{x}) &= \Pi(x)\times\Pi(y)\times\Pi(z) \end{aligned} \tag{9}$$

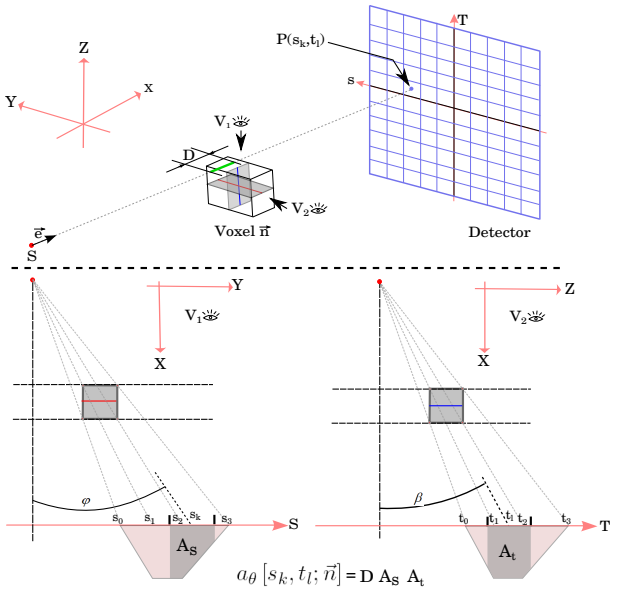

Fig. 2. Principle of the Separable Footprint method: Trapeze Trapeze SF-TT

where $\emptyset$ represents element-wise division, $\vec{\Delta} = (\Delta_x,\Delta_y,\Delta_z)$ is the grid-spacing, and Π represents the rectangular function. We also propose a separable model for the detector blur h :

$$h(s,t) = \frac{1}{\Delta_s\Delta_t}\left(\Pi\left(\frac{s}{\Delta_s}\right)\Pi\left(\frac{t}{\Delta_t}\right)\right) \tag{10}$$

Inspired by the shape of the true footprint $q(s,t;\theta;\vec{n})$ of the basis functions (eq.9) [3], with exploitation of the overlap area with the surface of each pixel, Yong Long et al. [3] have established a robust approximation of q (Fig.2) :

$$q(s,t;\theta;\vec{n}) \approx D \times trap(s;s_0,s_1,s_2,s_3) \times trap(t;t_0,t_1,t_2,t_3) \tag{11}$$

where $trap(a;b_0,b_1,b_2,b_3)$ is trapezoid function with b_0, b_1, b_3 and b_4 represent the vertices of the trapeze.
D is the voxel-ray-dependent amplitude [3] :

$$D = \frac{\Delta_x}{|\cos(\beta)| \times \max(|\cos(\varphi)|\,,|\sin(\varphi)|)} \tag{12}$$

The combination of the equations eq.8, eq.10, and eq.11, allows the computation of $a_\theta\,[s_k,t_l;\vec{n}]$:

$$\begin{aligned} a_\theta\,[s_k,t_l;\vec{n}] &= \int_{\Delta_s}\int_{\Delta_t} h(s_k - s, t_l - t)q(s,t;\theta;\vec{n})dsdt \\ &= D \times T(s_k - \tfrac{\Delta_s}{2}, s_k + \tfrac{\Delta_s}{2}) \times T(t_l - \tfrac{\Delta_t}{2}, t_l + \tfrac{\Delta_t}{2}) \end{aligned} \tag{13}$$

where T represents the overlap area with the pixel (the surface A_S and A_t in Fig.2).

2.3. Simplified Distance Driven Projector

The coefficient $a_\theta\,[s_k,t_l;\vec{n}]$ can be defined as the likelihood that one photon emitted by the voxel $\vec{n}$ will be detected by the pixel (s_k,t_l). Inspired by this definition, and the Distance Driven method [4], we proceed in three steps : 1) For each voxel $\vec{n}$, we compute the conical

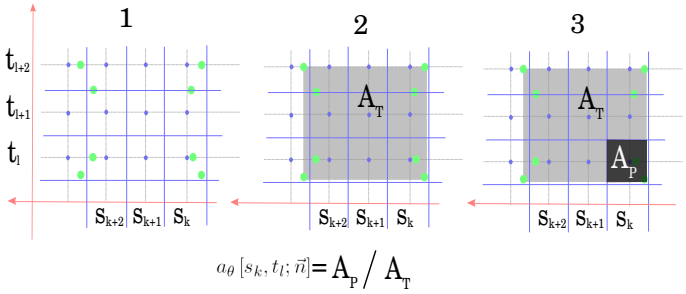

Fig. 3. Principle of Simplified Distance-driven method.

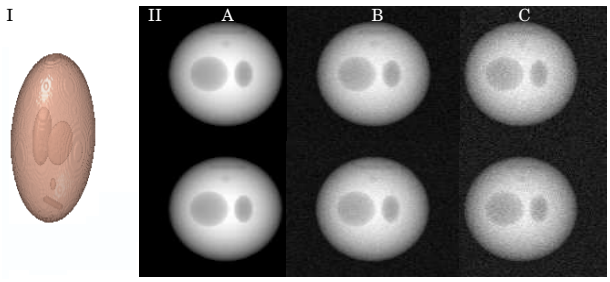

Fig. 4. Projection results. (I): binary 3D digital phantom. (II): projection results for $\theta = 0°$, Line 1: using SF-TT matrix, Line 2: using SDD matrix, column A: without noise, column B: with noise SNR_{VAR}=25 db, column C: with noise SNR_{VAR}=20 db.

projections of the eight cubic vertices (green dots in Fig.3).
2) We draw the smallest rectangle enclosing these projection points, and we can assume that the probability that a photon emitted by this voxel $\vec{n}$ will be detected in the rectangular surface (A_T in Fig.3) which is equal 1.
3) We calculate the overlap surface between each pixel and the rectangular area (A_P in Fig.3), and the coefficients of the projection matrix is inferred as a area ratio as : $a_\theta [s_k, t_l; \vec{n}] = {}^{A_P}/_{A_T}$

2.4. Model-Based Binary Reconstruction

To evaluate these computation methods of projection matrices and, in particular, their impact on reconstruction, we chose methods based only on minimizing a cost function which is a data attachment term without regularization: $E_d = \frac{1}{2} \|p - Af\|^2$.
Object-oriented methods assume that the reconstruction consists of a background region Ω_{out} and a foreground region, Ω_{in}, representing the object [9]. Consequently, in the case of a binary reconstruction, the data attachment term can be rewritten in as :

$$E_d = \frac{1}{2} \|p - f_{in} A\delta_{\Omega_{in}} - f_{out} A\delta_{\Omega out}\| \quad (14)$$

where f_{int} and f_{out} represent the intensity value of the background and the object respectively, and δ_{Ω_i} is the characteristic function of Ω_i. To optimize E_d, we adopt deformable models (precisely the level set methods), for which the velocity field V_d can be calculated by applying derivation tools of the form :

$$V_d = (f_{out} - f_{in}) A^T (p - Af) \quad (15)$$

The use of level set function make easy the determination of different regions Ω_i and their characteristic functions δ_{Ω_i}. The evolution equation is defined as : $\frac{\partial \psi}{\partial t} = V_d |\nabla \psi|$ f_{out} and f_{in} depend of δ_{Ω_i} and they are updated after each evolution of level-set function ψ [9].

3. RESULTS AND DISCUSSIONS

3.1. Projection Results

We simulated the X-ray cone-beam projections of a binary 3D Shepp-Logan phantom, which includes a sphere, a rectangular parallelepiped, and two ellipsoids (Fig.4.I). The digitization is performed in $N_X \times N_Y \times N_Z = 128 \times 128 \times 128$ voxels of size $\Delta_X = \Delta_Y = \Delta_Z = 1.2mm$. The flat-detector is simulated with a size of $N_s \times N_t = 128 \times 128$ cells spaced by $\Delta_s = \Delta_t = 2mm$, located at a distance $D_{sd} = 1103mm$ from the X-ray source. The whole "source-detector" rotates around a fixed Z-axis, such as $D_{so} = 690mm$.

In accordance with these acquisition parameters, projections are generated by implementing SF-TT, SDD and RD projectors, for different projection angles θ, such as $\theta \in \left[-\frac{\pi}{2}, +\frac{\pi}{2}\right]$. In order to study the noise influence on the reconstruction results, and have more realistic projection images, an additive Gaussian noise is introduced with different values of SNR_{VAR} (Fig.4.II).

3.2. Binary Reconstruction Results

The binary reconstruction is based on Object-oriented method, for which we have chosen deformable models to minimize a cost function based on data attachment term (eq.14). To quantify the quality of these reconstructions, we chose the criterion NMSE (Normalized Mean Square Error).
Firstly, we studied the convergence speed of each reconstruction, while varying projection operators (SF-TT, SDD and RD). For this first test series, we plot the NMSE of reconstruction for the first 100 iterations, when using 13, 7 or 5 projections (respectively columns A, B and C in Fig.5), and different noise levels SNR_{VAR}, without noise, 25dB, and 20dB (Lines 1, 2 and 3 in Fig.5). For each reconstruction, we chose the same initial coarse object (binary hollow sphere), and we initialized f_{out} and f_{in} at 1 and 3.
In a second step, we evaluated the reconstruction accuracy by varying the noise level from SNR_{VAR} =10 to 100 db, and the projection number (Fig.6.II). For this test series, we chose an initial object (Fig.6.I.B) which presents a rough approximation of our object (binarization of a Least Mean Square Error Reconstruction) after a few iterations), to be sure to achieve the optimal reconstruction.

3.3. Discussion

By analyzing Fig.5, we can say that in the case of level set initialization with a coarse object, and in the absence of noise, our binary reconstruction converges faster when using SDD projector, compared to SF-TT and RD projectors, and this speed appears faster when we decrease the number of projections. The fact of adding noise reduces this speed difference. Should note here that one iteration is defined as a reconstruction after having used whole projections (13, 7 or 5), and the jump that appears in NMSE curves (line 1) is due to the reconstruction of small structure (rectangular parallelepiped and sphere).
The results shown in Fig.6 prove that the reconstruction accuracy decreases with the increase of noise level and the decrease of number of projections. However, regardless of the operator used (SF-TT, SDD or RD), the reconstruction accuracy does not vary. Anal-

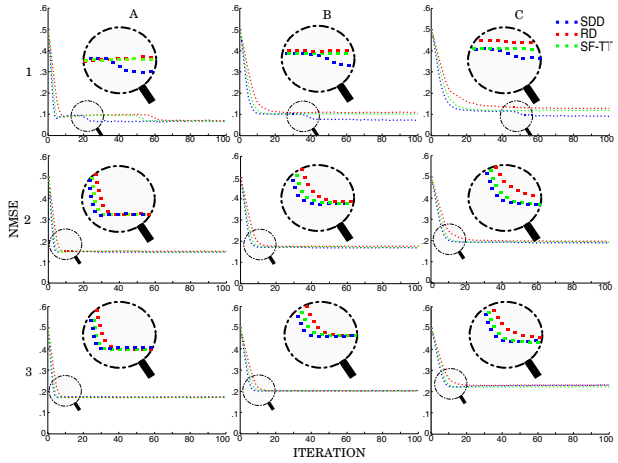

Fig. 5. NMSE according to iterations. line 1: without noise, line 2: withe noise SNR_{VAR}=25 db, line 3: withe noise SNR_{VAR}=20 db, column A: using 13 projections, column B: using 7 projections, column C: using 5 projections.

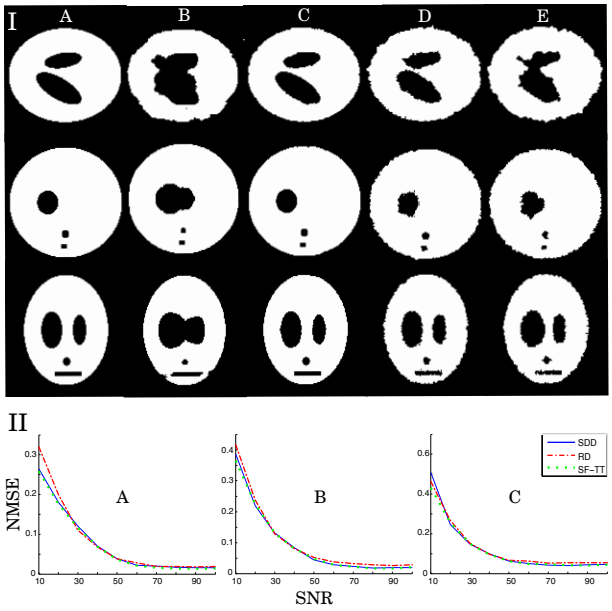

Fig. 6. (I): Binary reconstruction from five projections using SDD projector, visualization of the three central slices, column A: reference object, column B: initial object (obtained by LMSER reconstruction after few iterations), column C: reconstruction without noise, column D: reconstruction with noise $SNR_{VAR} = 25db$, column E: reconstruction with noise $SNR_{VAR} = 20db$. (II): NMSE according to SNR, A: reconstruction from 13 projections, B: reconstruction from 7 projections, C: reconstruction from 5 projections.

ysis of Fig.6 enables us to divide the results of the reconstruction in three groups: a first group for which the NMSE is less than 0.07 ($SNR_{VAR} \geq 50db$),where we can say that the reconstruction is good, a second group for which NMSE $\in [0.07, 0.25]$ ($20db \leq SNR_{VAR} < 50db$), where we have a weak reconstruction and we can hope to improve these results with a simple contour regularization, and finally, the last group for which NMSE is greater than 0.25 ($SNR_{VAR} < 20$) where the reconstruction is very bad, so the necessity of introducing high-level constraints.

3.4. Conclusion and perspective

We proposed a 3D object-based binary reconstruction without regularization based on a new simplified Distance-driven (SDD) projector and a level set approach which acts as an implicit regularizer. In this experiment, we studied the reconstruction quality using SF-TT, RD and SDD projectors in the case of noisy and sparse data from cone-beam acquisitions. A binary Shepp-Logan phantom was used for performance evaluation in varying the number of projections and the gaussian noise level. Considering the limited number of projections, there is no difference in the reconstruction accuracy term and convergence speed between these three approaches. However, our reconstruction converge faster when using SDD projector compared with the SF-TT and RD operators, in the absence of noise. The results show also a proportional degradation of the binary reconstruction with the increase of noise, and we have established preliminary classification on the limits of such reconstruction in presence of noise, and a limited number of projections. Future work will be oriented to find the best a priori, to compensate the degradation introduced by the noise, and to consider a gray-scale reconstruction.

4. ACKNOWLEDGMENTS

This work was supported by ANR grant MESANGE (ANR-08-BLAN-0198), the National Natural Science Foundation (No. 31100713) and French National Institute for Health (INSERM).

5. REFERENCES

[1] Hu, Y; Xie, L, Luo, LM; Nunes, JC; Toumoulin, C; "L0 constrained sparse reconstruction for multi-slice helical CT reconstruction", *Phys. in Med. and Biol., 56(4), 2011, pp. 1173-89.*

[2] Kim, JK; Fessler, JA, Zhang, Z "Forward-projection architecture for fast iterative image reconstruction in X-ray CT," IEEE Trans. Sig. Proc., 60(10):5508-18, 2012.

[3] Long, Y; Fessler, JA; Balter, JM "3D forward and back-projection for X-ray CT using separable footprints', IEEE Trans. Med. Imag., 29(11):1839-50, Nov. 2010.

[4] De Man, B; Basu, S "Distance-driven projection and backprojection in 3D", Phys. Med. Biol., vol.49, pp.2463-2475, 2004.

[5] Siddon, RL "Fast calculation of the exact radiological path for a three-dimensional CT array", Medical Physics, 12(2), pp.252-255, 1985.

[6] Joseph, PM "An Improved Algorithm for Reprojecting Rays Through Pixel Images", IEEE Trans. Med. Im., 1(3), pp. 192-196, 1983.

[7] Zhuang, W; Gopal, SS; Hebert, TJ "Numerical Evaluation of Methods for Computing Tomographic Projections", IEEE Trans. Nucl. Sci., 41(4), pp. 1660-1665, 1994.

[8] Zeng, G; Gullberg, G "A ray-driven backprojector for backprojection filtering and filtered backprojection algorithms", IEEE NSSMI Conf., pp 1199-1201, 1993.

[9] Gaullier, G; Charbonnier, P; Heitz, F "Introducing shape priors in object-based tomographic reconstruction," IEEE ICIP, 2009, pp.1077-1080, 2009.